Velocity-space studies of fast-ion transport at a sawtooth crash in neutral-beam heated plasmas

C M Muscatello[1], W W Heidbrink[1], Ya I Kolesnichenko[2], V V Lutsenko[2], M A Van Zeeland[3] and Yu V Yakovenko[2]

[1] Department of Physics and Astronomy, University of California-Irvine, Irvine, CA, USA
[2] Institute for Nuclear Research, Kiev, Ukraine
[3] General Atomics, PO Box 85608 San Diego, CA 92186-5608, USA

Abstract

In tokamaks the crash phase of the sawtooth instability causes fast-ion transport. The DIII-D tokamak is equipped with a suite of core fast-ion diagnostics that can probe different parts of phase space. Over a variety of operating conditions, energetic passing ions are observed to undergo larger redistribution than their trapped counterparts. Passing ions of all energies are redistributed, but only low-energy ($\lesssim 40$ keV) trapped ions suffer redistribution. The transport process is modeled using a numerical approach to the drift-kinetic equation. The simulation reproduces the characteristic that circulating energetic ions experience the greatest levels of internal transport. An analytic treatment of particle drifts suggests that the difference in observed transport depends on the magnitude of toroidal drift.

(Some figures may appear in colour only in the online journal)

1. Introduction

Among the many internal instabilities inherent to tokamak plasmas, sawteeth are periodic events occurring on large spatial scales without necessarily causing discharge disruption. Sawteeth were observed to cause internal redistribution of various species of fast ions: beam deuterium [1, 2], fusion-born proton and helium-3 [3], and both passing and trapped deuterium–tritium alphas [4, 5]. The velocity-space dependence of fast-ion transport by the sawtooth instability was studied previously on TFTR and TEXTOR. On TFTR, the pellet charge-exchange (PCX) and alpha-charge exchange recombination spectroscopy (α-CHERS) diagnostics obtained data on the redistribution of trapped and passing fast ions at a sawtooth crash [6]. A large depletion in the core passing-ion density was detected during a crash event with α-CHERS. The lack of core PCX data makes it difficult to assess the effect of sawteeth on the trapped energetic-ion population, but a broadening in the profile is observed. A more recent investigation on TEXTOR utilized a collective Thomson scattering (CTS) diagnostic during sawteeth to resolve the 1D fast-ion distribution function for various angles with respect to the magnetic field [7]. It was found that trapped energetic ions are less susceptible to sawtooth-induced transport than the passing population.

Differences between the effect of sawteeth on passing and trapped ions extend to the theoretical realm as well. Modeling of the redistribution of passing energetic ions invoking attachment to the evolving flux surfaces during the crash reproduces experimental results [4]. On the other hand, application of the flux-attached model to the trapped-ion population yields poor agreement with experiment [6]. To account for this difference, the theoretical works invoke two distinct transport mechanisms: transport by flux-attachment [4] (dominant for passing particles) and transport by $E \times B$ drift [6] (dominant for trapped particles). However, it can be shown that $E \times B$ drift and flux-attachment are cause and effect [8]; a particle that is well-situated near a flux surface moves with the surface by the $E \times B$ drift. Therefore, *any* particle attached to an evolving flux surface is prone to sawtooth-induced transport, but the frozen-in condition is broken by particles that experience strong toroidal drifts. To our knowledge, no previous publications have shown that toroidal drift effects lead to the measured transport differences.
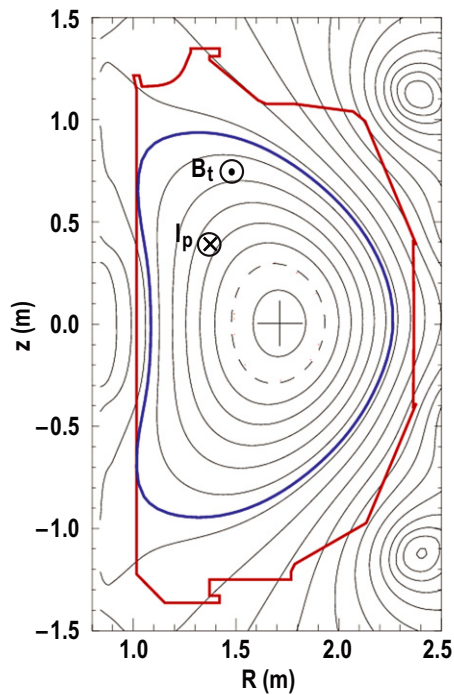
Figure 1. Poloidal cross-section of DIII-D for shot 141182. The thin contours are surfaces of constant magnetic flux; the dashed contour is the $q = 1$ surface; the inner thick contour (bean shape) is the last closed flux surface; the outer thick contour indicates the wall of the vessel.

In this paper, we present experimental data of velocity-spaced-resolved fast-ion signals during sawteeth on DIII-D. Consistent with previous results, we observe stronger redistribution of passing fast ions compared with their trapped counterparts. A drift-kinetic simulation is performed, and the results qualitatively agree with the observation that passing fast ions experience the greatest degree of redistribution. To remind the reader of the extensive theoretical work done in this subject, an abbreviated sketch of the important aspects of the theory will be presented. The theory associates the transport difference between passing and trapped fast ions to their magnitude of toroidal drift. A critical energy exists where toroidal drift plays a crucial role in the degree of transport. The critical energy can be represented in velocity space, dictating a redistribution boundary. We show that changes in the energy spectrum of fast ions are consistent with an analytic calculation of the redistribution boundary. The paper is organized as follows. In section 2 we present our experimental setup and data. Section 3 summarizes the results from our simulations and includes an analytic sketch of particle drifts. Our concluding remarks can be found in section 4.

2. Experimental setup and results

With its extensive suite of diagnostics, neutral-beam injection system, plasma control system, and array of magnetic field shaping coils, the DIII-D tokamak [9] is a highly versatile and well-diagnosed machine. The focus of the first part of this section is an analysis of fast-ion data for similar DIII-D shots 141182 and 141195. Figure 1 is an elevation

of the plasma cross-section for shot 141182 as calculated by the equilibrium reconstruction code EFIT [10]; the magnetic axis is $R_{\text{axis}} = 1.72$ m. The motional Stark effect (MSE) polarimeter [11] measures the pitch of the local magnetic field. MSE is utilized to constrain the safety factor (q) profile and equilibrium reconstruction. The dashed flux surface indicates the location of the $q = 1$ surface (normalized toroidal flux $\rho \approx 0.3$) just before a crash. The plasma current I_{p} and toroidal field B_{t} are 1.3 MA and 1.9 T, respectively. In these discharges, I_{p} is directed counter-clockwise, and B_{t} is clockwise viewed from the top of the tokamak (so that the ion ∇B drift is downward). A time history of shot 141182 is shown in figure 2. The top trace is the electron temperature T_{e} measured by the central electron cyclotron emission (ECE) channel at the midplane [12]. The middle trace is the neutron emission measured by a plastic scintillator located about $30°$ above the midplane [13]. The bottom trace is the fluctuations of the magnetic field measured by a Mirnov coil at the midplane. The average sawtooth period and amplitude (defined as $|T_{\text{e precrash}} - T_{\text{e postcrash}}|/T_{\text{e precrash}}$, and determined by the central ECE channel) are 85 ± 5 ms and 0.35 ± 0.02, respectively. Precrash and postcrash plasma profiles are plotted in figure 3. Ion temperature, toroidal rotation velocity and main impurity (carbon) density are inferred from the charge-exchange recombination (CER) diagnostic [14]. The precrash/postcrash profiles are generated by averaging 10 ms before/after five consecutive sawtooth crashes. Random errors are calculated using the ensemble standard deviation. The fast-ion population is generated through deuteron neutral-beam injection at an average full injection energy of 75 keV. Four neutral-beam sources are modulated on and off for diagnostic background subtraction and for the purpose of reducing the overall power to keep the discharge in L-mode. The average full injection energy is calculated by weighting the injection voltage of each source according to its duty cycle. Sawtooth repeatability is necessary for fast-ion profile reconstruction prior to and following a crash. Long time domains (≈ 1 s) of uniform sawteeth are produced in order to obtain average precrash and postcrash profiles with sufficient statistics. During the sawtoothing portion of all discharges discussed here, no other MHD activity such as Alfvén eigenmodes, fishbones or tearing modes is detected.

DIII-D has an extensive fast-ion diagnostic suite that probes different regions of phase space. Fast-ion deuterium-alpha (FIDA) is the main diagnostic technique used in this paper to measure the confined fast-ion profiles [15]. At the time of writing, three sets of FIDA collection optics are currently in use at DIII-D. They are named according to the geometry of their sightlines in the tokamak. Projections of the sightlines for the three installations are shown in figure 4 in two different planes: figure 4(*a*) shows the poloidal plane (at fixed toroidal angle) and figure 4(*b*) the plan view at the midplane ($z = 0$). The active collection volume of the any sightline is the intersection of the sightline with the neutral beam. In figure 4(*a*) the vertical extent of a neutral beam is indicated by the horizontal gray lines. In figure 4(*b*) the beam trajectory in the midplane is indicated by the gray swatches. Each viewing
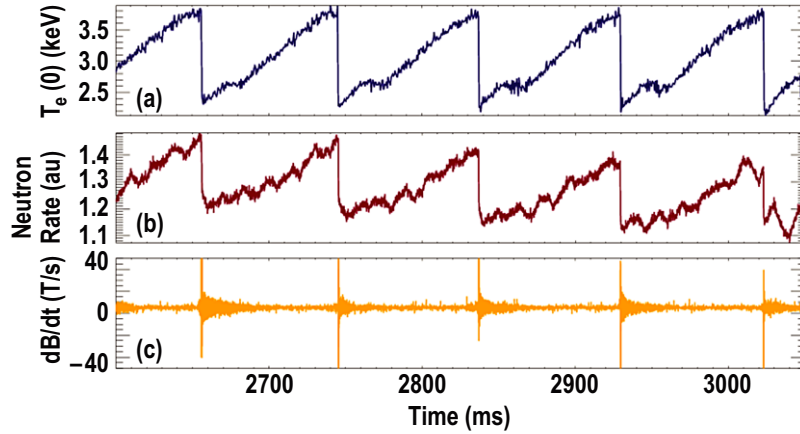
Figure 2. Time slice from shot 141182. (*a*) Central electron temperature (T_e) measured by the ECE diagnostic; (*b*) neutron emission measured by a scintillator; (*c*) magnetic fluctuations measured by a Mirnov coil.
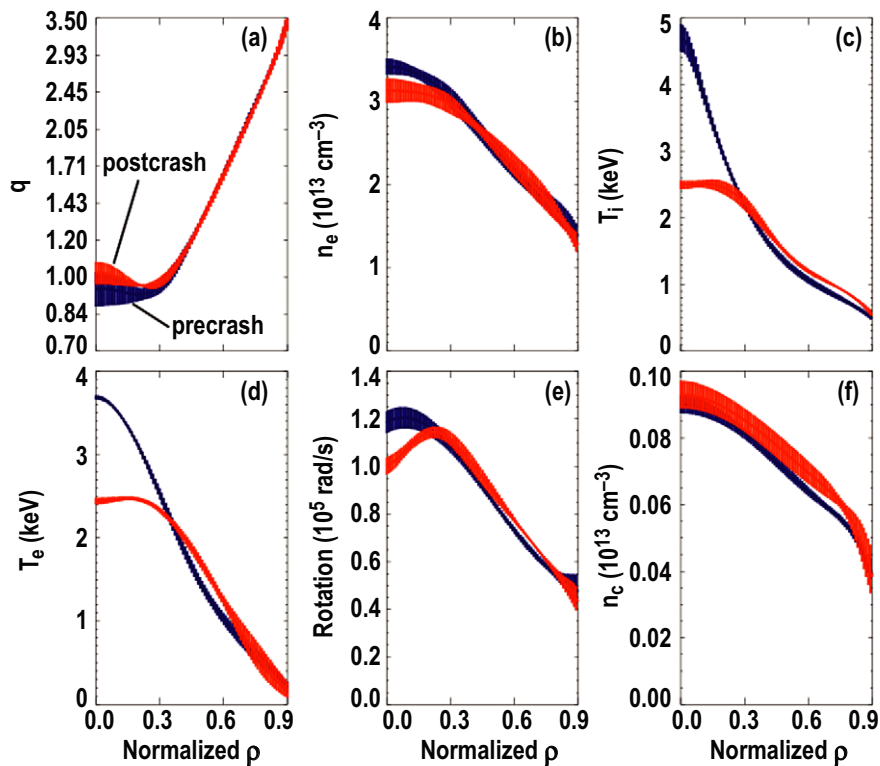

Figure 3. Precrash (dark blue) and postcrash (orange) profiles for (*a*) safety factor, (*b*) electron density, (*c*) ion temperature, (*d*) electron temperature, (*e*) toroidal rotation, (*f*) main impurity (carbon) density. Random errors from ensemble averaging are indicated by the thickness of the profile plots.

chord of a spectroscopic FIDA system measures the photonic D_α spectrum produced by a population of deuterium ions that undergo charge-exchange with injected neutral deuterons. The unshifted wavelength λ_0 of a D_α photon is 656.1 nm. However, a photon emitted from a moving source is Doppler shifted depending on the velocity of the source. More specifically, the Doppler shift $\Delta\lambda$ depends on the dot product of the velocity of the moving source and the direction vector of the emitted photon. Therefore, $\Delta\lambda$ depends on the energy of the moving source along the emitted photon direction; let us call this energy E_λ. FIDA measures the D_α spectrum and each value of wavelength thus corresponds to an E_λ value. For FIDA, E_λ translates to the fast-ion energy component parallel to the

diagnostic sightline. Therefore, ions with various values of pitch ($\chi \equiv V_\parallel / V$ where $V_\parallel$ is the ion velocity component parallel to the magnetic field) and total energy E can contribute to a measured fast-ion energy E_λ of the spectrum. This leads to an instrumental weighting in fast-ion phase space depending on several factors described in [16].

To produce FIDA spatial profiles, spectra from each radial chord are integrated over a particular wavelength band. These values are then divided by the local neutral density to produce profiles which are approximately proportional to the fast-ion density. The neutral density calculation approximates the ionization cross-section given plasma density, plasma temperature, plasma toroidal rotation and impurity density
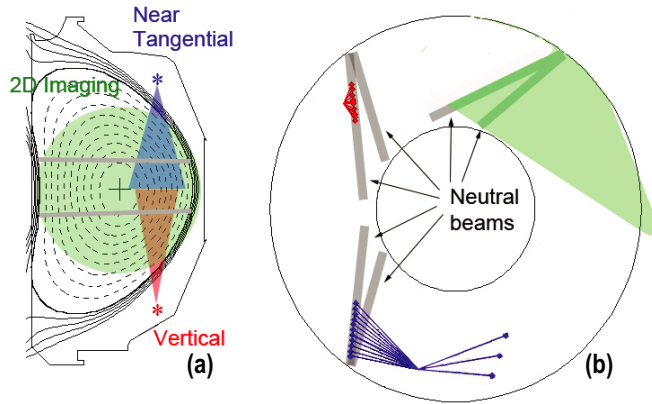
Figure 4. Projections of the FIDA sightlines for three different optical installations. (*a*) Poloidal plane at a fixed toroidal angle. Horizontal gray lines indicate the approximate vertical extent of the neutral beam. (*b*) Plan view from the top of the tokamak. Gray swatches indicate beam trajectories in the midplane.

profiles. The profiles are spline fits to experimental measurements. In addition to the profiles, the neutral density calculation also requires values for the injected neutral-beam power and the full, 1/2 and 1/3 energy species fractions. Errors in the profiles, reported injected power, and species mix propagate to errors in the calculated neutral density. The dependence of the neutral density uncertainty on the errors of the input parameters can be determined by independently adjusting the parameter values. Out of all the plasma profiles, the neutral deposition is most sensitive on the plasma density profile. A reduction in the plasma density profile by 10% negligibly affects the neutral density at the edge but increases it in the core by 10%. Inaccurate plasma density profile modeling can lead to unsystematic uncertainties in the calculated neutral density. A reduction in the injected power by 10% reduces the neutral density by 10% uniformly across the beam trajectory. Fortunately, uncertainty in the reported injected power value is a systematic error which does not affect relative comparisons. A reduction in the full-energy species fraction by 10% negligibly reduces the neutral density by 5% uniformly across the beam trajectory. Therefore, uncertainties in the plasma density profile are likely the largest source of error. In the cases studied here, errors in the electron density profile are determined by a Monte Carlo method and yield values of less than 10% across the profile.

Figure 5 shows the weight functions that represent the contribution to the FIDA signal when the spectrum is integrated between energies $E_\lambda = 30$ and $60\,keV$ for the spectroscopic FIDA systems currently on DIII-D. Figures 5(*a*) and (*b*) depict the instrumental weight functions in velocity-space for two spectroscopic FIDA systems, the vertical [15] and near-tangential [17] instruments, respectively. DIII-D is also equipped with an imaging system that detects a two-dimensional poloidal cross-section of the fast-deuterium profile when used in conjunction with a narrowband interference filter [18]. The bandwidth is ≈4 nm centered on $\lambda = 652\,nm$ which corresponds to $E_\lambda = 10$–$80\,keV$. The FIDA imaging weight function is shown in figure 5(*c*). Although FIDA integrates much of the velocity space, the

viewing geometries of the three systems skew the coverage differently. Comparing the three, the instrument function of the vertical system is nearly symmetric about particle pitch of zero and strongly weighted about zero. The nearly tangential system is heavily weighted toward large positive values of pitch, while 2D FIDA weights large negative values of pitch most heavily. The sign of the pitch indicates the direction of the particle parallel motion with respect to the I_p direction, where negative values indicate opposite direction to I_p. The overlaid dashed lines indicate fast ion trapped/passing boundaries that are calculated using a guiding-center orbit integration tool (see the appendix of [19]). These plots demonstrate the practicality of using the three systems to investigate the different dynamics of fast ions with varying orbit types.

In order to obtain high quality fast-ion signals, the discharges are chosen to be low-density L-mode deuterium plasmas. The signal-to-noise ratio of the FIDA signal is poor for line-averaged densities above ~7 × 10^{19} m^{-3}, and edge-localized modes (ELMs) introduce scattered light into the diagnostic, contaminating the spectra. In addition, simultaneous data acquisition during the same shot was desired for the two spectroscopic systems. Therefore, careful beam programming must be employed; otherwise, the vertical system's diagnostic beam can contaminate the tangential system's signal (and vice versa), inhibiting proper background subtraction. The beam programming on shot 141182 was set up so the beams were interleaved with intervals where both diagnostic beams are off for background subtraction. Average precrash and postcrash spectra are generated by averaging over many sawtooth cycles. For the vertical and near-tangential systems, spectra from various radial locations within the first and last 10% of each sawtooth cycle are chosen. Obtaining the desired FIDA spectra requires a background subtraction procedure described in [15], as shown schematically in figure 6. An ensemble of active (beam-on) spectra and background (beam-off) spectra are collected for precrash and postcrash phases. The average precrash and postcrash spectra are calculated by subtracting the average background spectrum from the average active spectrum. This subtraction technique assumes that the background spectrum is insensitive to the crash event. However, it has been observed that a sawtooth crash can cause changes in the background D_α signal [15]. On shot 141182, a passive D_α filterscope indicates that the background signal jumps less than 10% following a crash. Spectra from the tangential and vertical systems for a radial chord intersecting the midplane at $R = 186\,cm$ are shown in figure 7. Random errors from ensemble averaging are the largest source of uncertainty in these spectra. The average error in the vertical spectra is ~20% of the signal and ~10% in the tangential spectra. Evidently, ions in the entire measured spectral range of the tangential system are redistributed, while there appears to be an energy dependence in the redistribution measured by the vertical system. The dashed vertical line ($\lambda = 652\,nm$, $E_\lambda = 36\,keV$) indicates the maximum Doppler shift where deviations between the precrash and postcrash spectra are observed by the vertical system.

To generate spatial profiles from the spectroscopic systems, integration of the spectrum from each radial chord
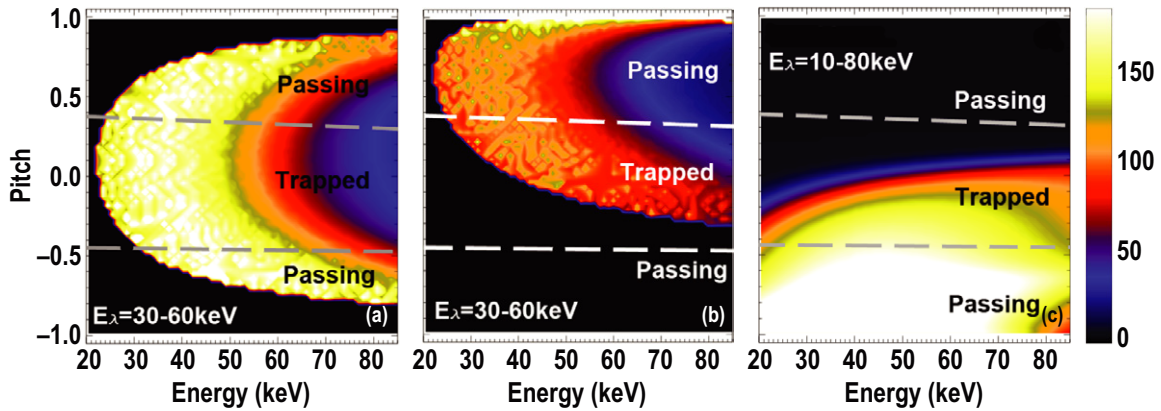
Figure 5. Instrumental weight functions of FIDA. Horizontal dashed lines indicate trapped/passing boundaries calculated by an orbit-following guiding-center code. (*a*) Vertical instrument function for a spectral integration of 30 to 60 keV. The viewing chord crosses the neutral beam at the midplane and major radius $R = 183$ cm. (*b*) Tangential instrument function for a spectral integration of 30 to 60 keV. The viewing chord crosses the neutral beam at the midplane and major radius $R = 181$ cm. (*c*) 2D FIDA instrument function for a bandpass integration of 10 to 80 keV. The viewing chord crosses the neutral beam at the midplane and major radius $R = 181$ cm.
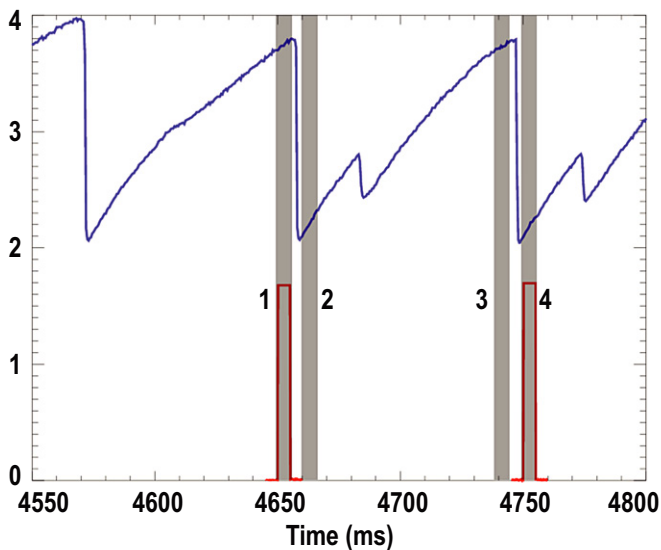

Figure 6. Schematic of conditional averaging and background subtraction technique. The sawtooth signature of the core ECE channel for shot 141182 is shown. Vertical swatches indicate times chosen to be postcrash and precrash ($\pm 10\%$ about sawtooth crash) times. The active FIDA neutral-beam trace is overlaid (slices 1 and 4). Background subtraction is performed by taking the average beam-on signals and subtracting the average beam-off signals. Precrash FIDA signal = (signal from slice 1)–(signal from slice 3). Postcrash FIDA signal = (signal from slice 4)–(signal from slice 2).

is performed over a wavelength range corresponding to E_λ of 30–60 keV. The 2D imaging system was not configured for shot 141182, so a repeat shot 141195 was taken. For the imaging system, the bandpass filter provides *in situ* energy integration, and for shot 141195 the E_λ band is $\sim$10–80 keV. With the ensemble of energy-integrated FIDA values at each spatial location, average values and standard deviations for the precrash and postcrash phases can be calculated. The ensemble of energy-integrated spatial points for the precrash and postcrash phases includes both beam-on and beam-off signals. The FIDA signal for one radial location is found by subtracting the average beam-off signal from the average

beam-on signal, and this is done for both precrash and postcrash phases. An average precrash profile and an average postcrash profile are then generated, and these are used to assess the average redistribution induced by a crash. Figure 8 shows the average precrash and postcrash fast-ion profiles from the vertical, near-tangential and 2D FIDA systems. It is clear from these plots that there is a large depletion in the core fast-ion density induced by a sawtooth crash. Atomic cross-sections and collisional rates complicate absolute comparisons of the fast-ion profiles among the different systems, so we resort to relative comparisons. A simple fractional change calculation is used to compare the levels of transport during a typical sawtooth crash. Here, the fractional change is defined as, $f \equiv$ (postcrash signal – precrash signal)/(precrash signal). Figure 9 is a plot of f versus major radius R for the three systems. Evidently, the magnitude of the redistribution is different depending on the type of fast-ion orbit detected. We see from figure 9 that a larger drop is experienced by the fast ions detected by the near-tangential and 2D systems compared with those detected by the vertical system. 2D FIDA and the near-tangential array (sensitive to mostly counter-current passing and co-current passing ions, respectively) measure a similar percentage drop ($\sim$50%), which is significantly greater than the reduction ($\sim$25%) measured by the vertical system (sensitive largely to trapped ions).

Interpretation of changes in the FIDA spectra is complicated. FIDA radiation emitted by a volume in the plasma is approximately proportional to $n_f n_n \langle \sigma v_{rel} \rangle$ where n_f is the local fast-ion density, n_n is the local neutral density and $\langle \sigma v_{rel} \rangle$ is the average rate for generating neutrals in the $n = 3$ quantum state. Since n_n and $\langle \sigma v_{rel} \rangle$ depend on plasma parameters such as electron temperature T_e, ion temperature T_i, electron density n_e, toroidal rotation velocity v_{rot} and impurity density n_c, it is conceivable that any of these quantities can contribute to changes in the measured FIDA signal at a sawtooth crash. To estimate the contribution of changes in the plasma profiles on the measured FIDA signal during a sawtooth crash, we perform forward modeling with the FIDAsim code [20]. First we generate equilibrium
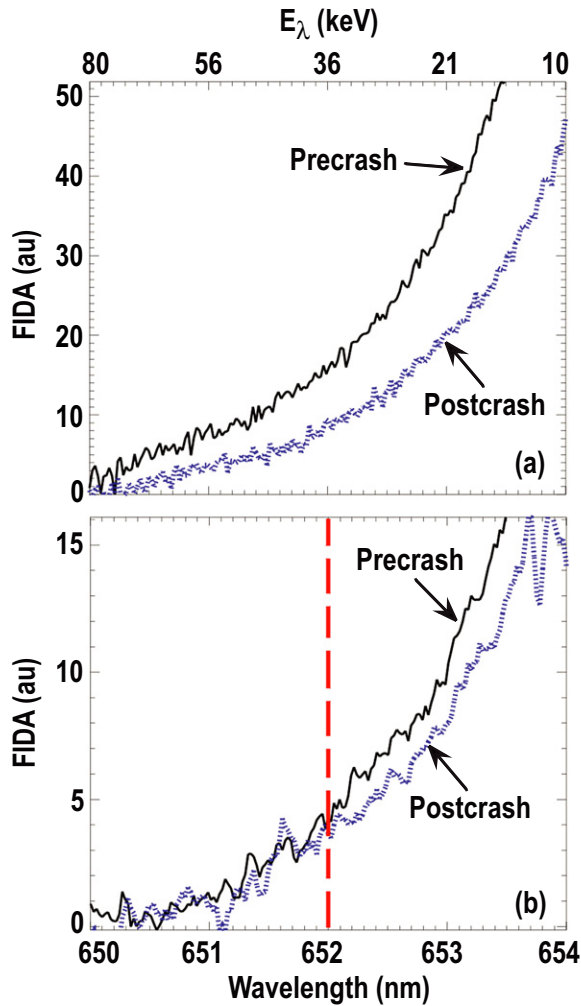
Figure 7. Conditionally averaged precrash and postcrash spectra versus wavelength (bottom abscissa) and corresponding E_λ (top abscissa) from the (*a*) near-tangential system (dominantly co-passing) at $(R, z) = (181, 0)$ cm and (*b*) vertical system (dominantly trapped) at $(R, z) = (183, 0)$ cm. The dashed vertical line corresponds to the maximum Doppler shift at which changes are seen in the vertical spectrum. Apparently, only fast ions with $E_\lambda < 36$ keV detected by the vertical system and all fast ions detected by the near-tangential system are affected by the crash.

reconstructions using EFIT just before and just after a typical sawtooth crash. Profiles are then fit to experimental data for T_e, T_i, n_e, v_{rot} and n_c. Next, we model the precrash and postcrash fast-ion distribution functions using the NUBEAM module [21] of TRANSP [22]. NUBEAM calculates the guiding-center drift orbit during the slowing-down process, handling various collisional and atomic physics. Among the outputs, the distribution function is calculated assuming toroidal axisymmetry. Although TRANSP includes the option to enable a generalized Kadomtsev sawtooth model, for the following analysis, the model is not used. This is appropriate for this sensitivity analysis since we are only concerned with the effect of the plasma profiles on the FIDA signals. Finally, the equilibrium data, plasma profiles and distribution functions are used as inputs to the FIDAsim code. The simulation predicts a fractional change in $n_n \langle \sigma v_{rel} \rangle$ of $0 > f > -0.15$ in the core channels of the tangential and vertical FIDA profiles
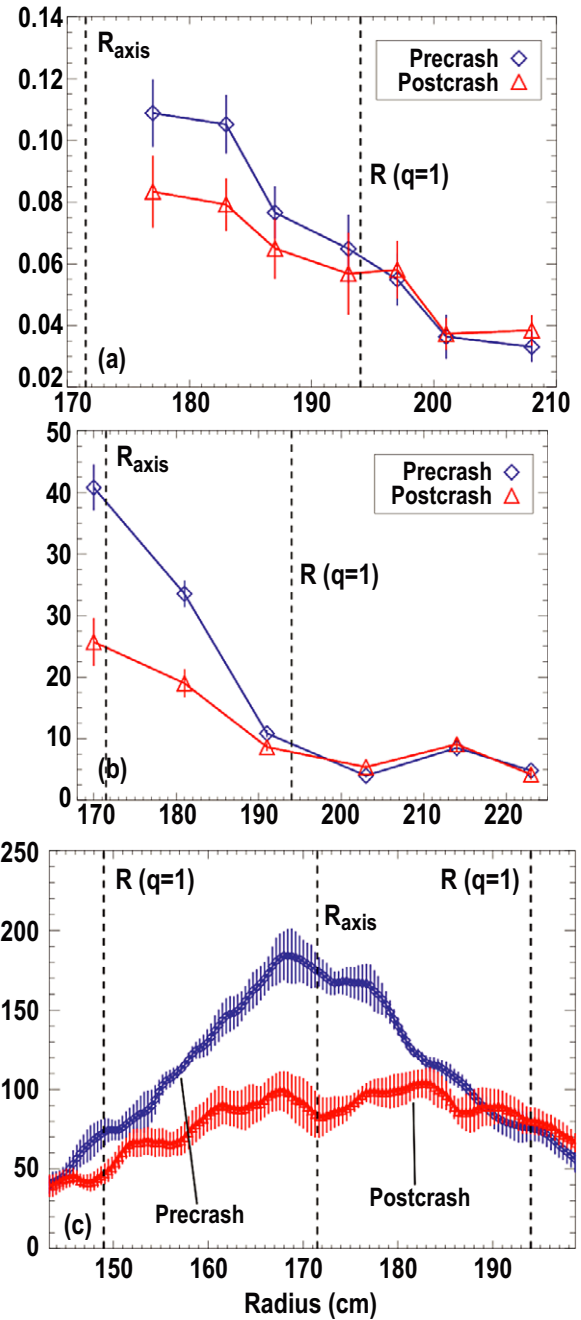

Figure 8. Radial profiles at the midplane proportional to the fast-ion density just before and just after an average sawtooth crash. The major radii of the magnetic axis and the $q = 1$ surface are denoted. (*a*) Trapped fast ions (detected by the vertical FIDA system). (*b*) Co-circulating fast ions (detected by the near-tangential FIDA system). (*c*) Counter-circulating fast ions (detected by the FIDA imaging system). The 1D radial profiles from the imaging system are extracted from pixels that detect signal along the midplane.

during a sawtooth crash assuming no fast ion loss. To estimate f of the fast-ion density, we assume the FIDA signal is exactly proportional to $n_f n_n \langle \sigma v_{rel} \rangle$ and the fractional change of $n_n \langle \sigma v_{rel} \rangle$ is -0.15. Under these assumptions, the fractional change of the fast-ion density measured by the tangential system is -0.41 and -0.12 measured by the vertical system. Similarly for 2D FIDA, modifications to the plasma profiles during the sawtooth crash can lead to observed changes in
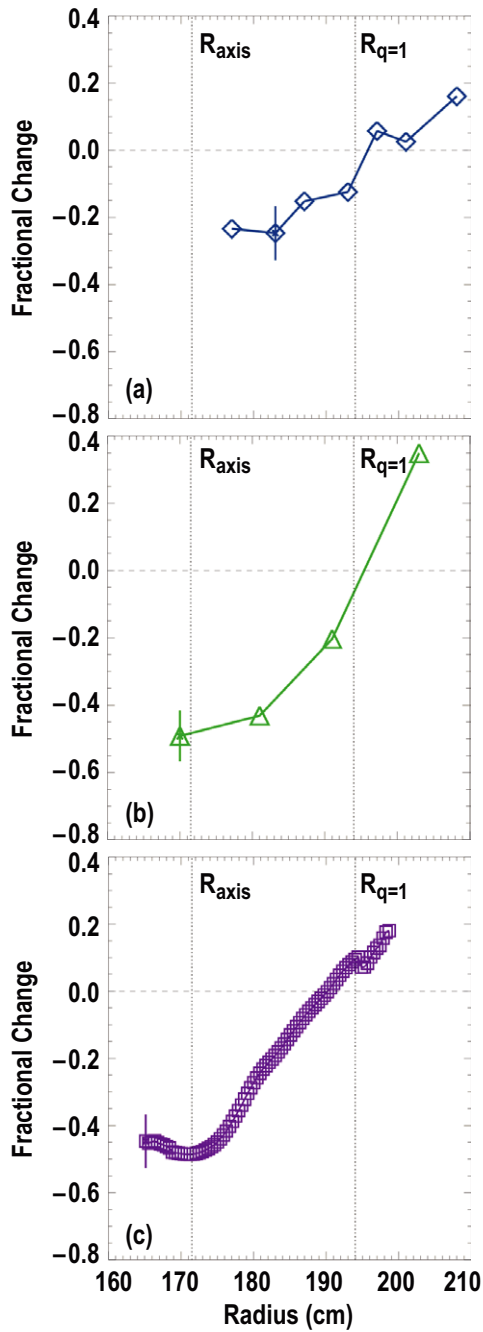
Figure 9. Fractional redistribution of fast-ion density at the midplane during an average sawtooth crash on shot 141182 for the three FIDA systems. (*a*) Trapped fast ions (detected by the vertical FIDA system). (*b*) Co-circulating fast ions (detected by the near-tangential FIDA system). (*c*) Counter-circulating fast ions (detected by the FIDA imaging system). The major radii of the magnetic axis and the $q = 1$ surface are denoted.

the measured FIDA profile. Furthermore, the average thermal ion temperature in the core just before a crash is 4.7 keV and follows a Maxwellian distribution function. Therefore, the low-energy cutoff of the bandpass filter ($\sim$10 keV) could allow 2D FIDA to pick up signal from particles in the wings of the thermal ion distribution function. In order to estimate the contribution of changes in the plasma profiles to the changes in the 2D FIDA signal, we utilize the same forward-
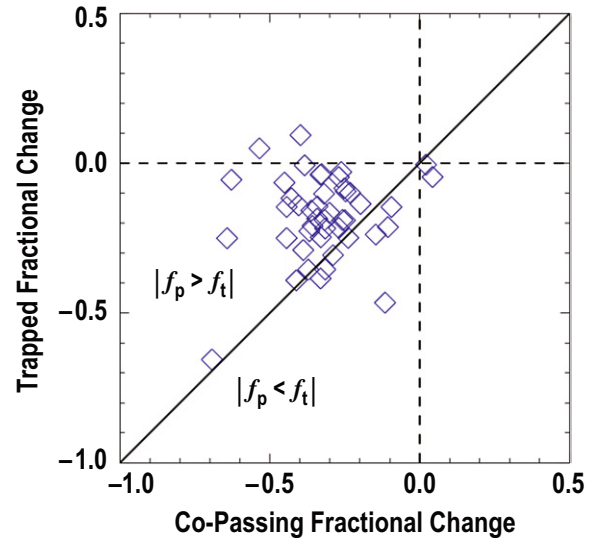
Figure 10. Scatter plot of f_{trapped} versus $f_{\text{co-passing}}$ using the central-most FIDA channels for 56 various plasma conditions. The diagonal line plot indicates $f_{\text{trapped}} = f_{\text{co-passing}}$. $\langle f_{\text{trapped}} \rangle = -0.17$ and $\langle f_{\text{co-passing}} \rangle = -0.32$.

modeling technique described above. The simulation predicts the fractional change of $n_{\text{n}} \langle \sigma v_{\text{rel}} \rangle$ to be $0 > f > -0.20$ in the core pixels of the 2D profile during a sawtooth crash. This suggests the fractional change of the counter-passing fast-ion density during the crash is -0.38.

Generalizing our previous single-shot analysis, we now turn to a database of shots documenting various different plasma conditions and cross-sectional shapes. All discharges in the database are L-mode plasmas. B_{t} and I_{p} range between 1.86–2.05 T and 1.16–1.34 MA, respectively. Average sawtooth periods and amplitudes span 48–108 ms and 0.21–0.37, respectively. Central precrash values of T_{e} and n_{e} range between $\sim$2.0–5.0 keV and $\sim(2.0$–$4.0) \times 10^{19}$ m^{-3}, respectively. Shots in the database include circular, bean-shaped, oval and 'D'-shaped plasmas. Shot data with good FIDA statistics are loaded into a database, and the fractional change f for the vertical and near-tangential systems is calculated for each condition. The results are presented in figure 10 as a scatter plot of f_{trapped} versus $f_{\text{co-passing}}$ for the radial chord closest to the magnetic axis ($R = 175$ cm). The diagonal line plot denotes $f_{\text{trapped}} = f_{\text{co-passing}}$. The region of the plot where $|f_{\text{co-passing}}| > |f_{\text{trapped}}|$ is far more populated than $|f_{\text{co-passing}}| < |f_{\text{trapped}}|$; average values of $f_{\text{co-passing}}$ and f_{trapped} are -0.32 and -0.17, respectively. We conclude that, under the conditions studied here, the observation of stronger transport of passing fast ions compared with trapped fast ions generally holds.
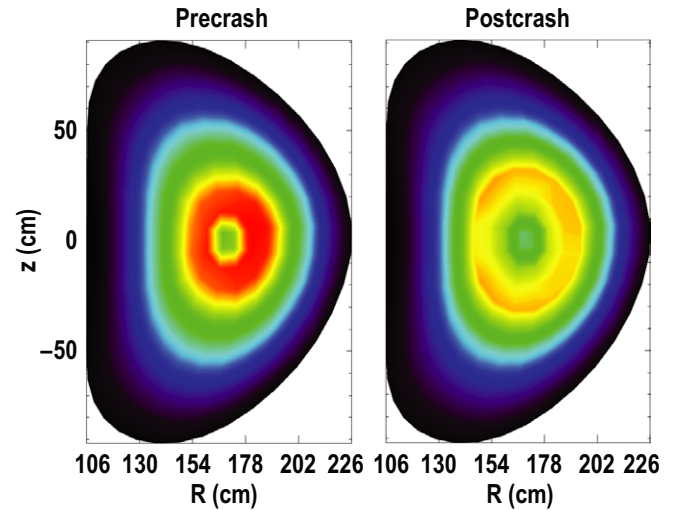
3. Theoretical discussion

Simulations to predict transport levels on DIII-D were carried out for shot 141182 using the theory described in [23]. Since fast-ion collision times O(100 ms) are much longer than the crash duration O(10 μs), collisions are not a significant contribution to modifications of the
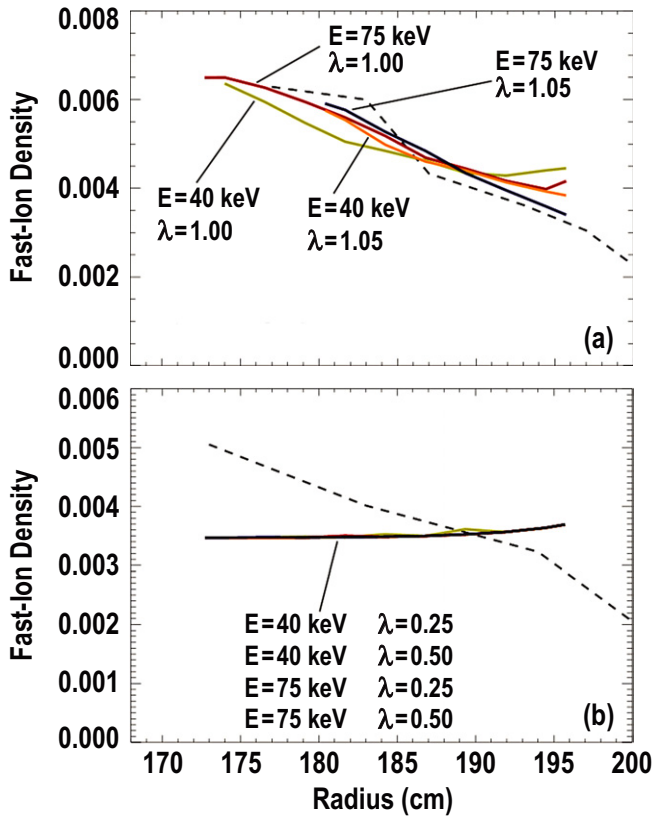
Figure 11. Measured precrash fast-ion profiles from FIDA (dashed) and simulated postcrash profiles (solid colored lines) for various values of energy E and $\lambda \equiv \mu B_0/E$ for (*a*) trapped and (*b*) passing particles.

Figure 12. Poloidal cross-section of beam-ion distribution predicted by TRANSP integrated over fast-ion energy $E > 20\,\text{keV}$. Left: distribution 5 ms before crash. Right: distribution 5 ms after crash. The same color scale applies to both images.
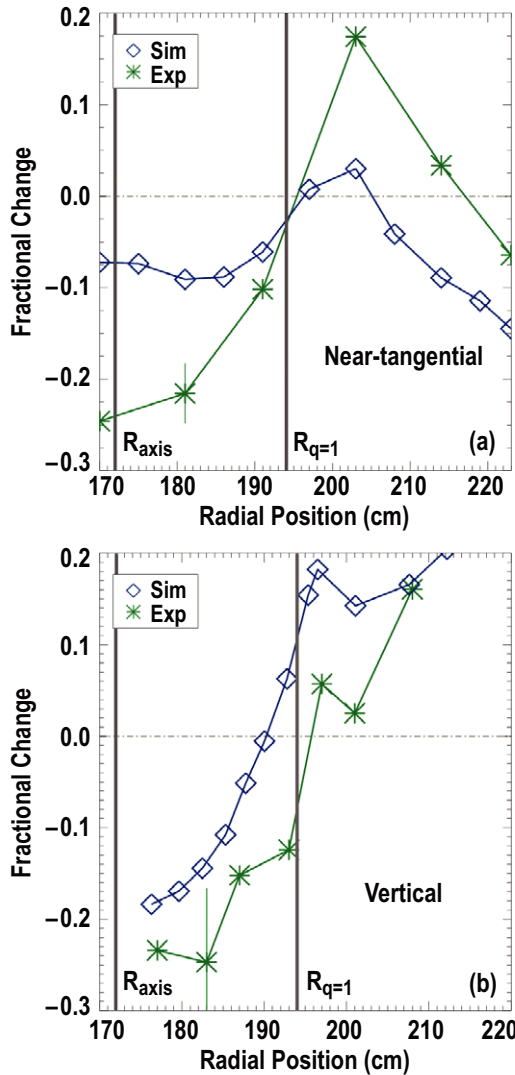
fast-ion distribution function during the crash. Therefore, the energetic-ion dynamics can be described by their guiding centers through a collisionless poloidal bounce/transit-averaged drift-kinetic equation. The OFSEF (Orbit Following in Sawtooth Electromagnetic Fields) simulation code based on the numerical procedure outlined in [23] solves the bounce-averaged Fokker–Planck equation. The code requires information characterizing the precrash state of the plasma. It then evolves the plasma state during a sawtooth crash according to the conventional Kadomtsev model [24]. OFSEF is supplied with precrash data from experimental measurements: the fast-ion density profiles from FIDA, the q-profile and plasma shape from MSE-constrained EFIT reconstructions, and plasma pressure profile from spline-fitted n_e, T_i and T_e measurements. The simulation follows the distribution of fast particles with specified values of total energy E and magnetic moment μ. For the case studied here, only four different combinations of E and μ for passing particles and four different combinations of E and μ for trapped particles were simulated. The goal simply is to demonstrate qualitatively the sawtooth-induced transport dependence on these variables. TRANSP simulations using the full distribution function (including synthetic FIDA diagnostic results) to predict sawtooth-induced transport will be described later. Figure 11 shows OFSEF simulation results for the supplied precrash trapped and passing fast-ion profiles. Postcrash profiles are plotted for select values of $\lambda \equiv \mu B_0/E$ and E (B_0 is the magnetic field on
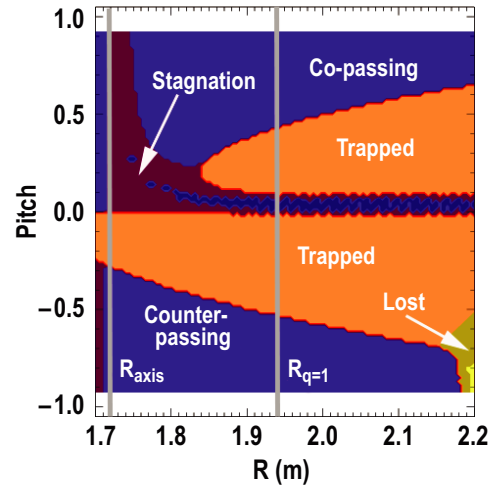
axis). The parameter λ can be thought of as the normalized perpendicular energy, but instead of taking the field at the particle location, the field on axis is used so that λ is a constant of motion. The simulation reproduces the characteristic that all core passing fast ions experience strong redistribution regardless of E and λ. However, for the trapped particles, their postcrash profile depends sensitively on E and λ; small values of E and λ produce the flattest postcrash profiles. Evidently, redistribution of trapped particles (with energies $\lesssim 80\,\text{keV}$) depends on the particle energy and pitch.

Results from figure 11 suggest that the severity of sawtooth-induced transport depends on the orbit characteristics of a fast ion. Due to the design of the OFSEF code referred to in the previous paragraph, it is difficult to perform simulations over the entire distribution function. For these purposes, we employ TRANSP which includes an option to turn-on redistribution by sawteeth. The TRANSP simulation is performed for shot 141182 over a period of time that includes eight relatively uniform sawteeth, each one with a period of approximately 80 ms. TRANSP is provided with EFIT equilibrium reconstructions and spline fits to experimental plasma profiles; the input data are chosen at equally spaced intervals of 15 ms, but TRANSP interpolates the input data between the user-supplied times on a 1 ms time interval. Sawtooth events are explicitly assigned, and TRANSP uses these times to apply the Kadomtsev sawtooth mixing model. One major caveat with the TRANSP sawtooth mixing model is that kinetic effects are not considered. All fast ions are treated thermally and redistributed according to the rearrangement of flux surfaces. The NUBEAM module is called to calculate the beam-ion distribution function 5 ms before and 5 ms after each sawtooth event. As a check that the TRANSP sawtooth model redistributes fast ions, the average distributions (averaged over fast-ion energies $E > 20\,\text{keV}$) before and after a crash are compared. Figure 12 is the spatial distribution of fast ions predicted by TRANSP before and after a crash event. Precrash and postcrash distribution functions from TRANSP are used

Figure 14. Orbit classifications versus pitch and major radius (at the midplane) for full-energy (75 keV) beam ions. The magnetic axis and radius of $q = 1$ surface are denoted.

Figure 13. Fast-ion density fractional change profiles showing experimental profile (green asterisk) and modeled profile (blue diamond) predicted by FIDAsim and TRANSP. The magnetic axis and radius of $q = 1$ surface at the midplane are denoted. (*a*) Near-tangential system sensitive mainly to co-passing particles. (*b*) Vertical system sensitive mainly to trapped particles.

as input to the synthetic diagnostic FIDAsim code to predict changes to the FIDA signal during a sawtooth crash. The results are shown in figures 13(*a*) and (*b*) for the vertical and near-tangential FIDA systems. It is clear that the simplified sawtooth model in TRANSP underestimates the magnitude of the change in density. The sawtooth crash in TRANSP is modeled after the conventional Kadmotsev theory; surfaces with like-valued helical flux inside and outside $q = 1$ reconnect and form a new unified surface. This process continues until q on-axis is restored greater than or equal to one, flattening the q, density and temperature profiles inside the mixing radius (largest minor radius at which reconnection occurs). If, in reality, the magnetic surface rearrangement during the crash differs substantially from the Kadomtsev process, there is no reason to believe that the effect on particle mixing should be the same. However, although there is a discrepancy in the absolute magnitude of the change in density between

the TRANSP Kadomtsev model and the data, the shapes of the redistribution profiles (the fractional change profiles) agree well. Compare the shapes of the fractional change profiles between simulation and experiment for the near-tangential FIDA system in figure 13(*a*). The inversion radius (inner most zero crossing, $R = 195$ cm) and the positive peak in the density change ($R = 203$ cm) are consistent. Also compare the results from the vertical FIDA system in figure 13(*b*). The profiles are monotonically increasing from the axis to $R = 196$ cm where a small dip in the profile occurs, resolved both synthetically and in the experiment. The relative consistency between the simulation and experiment suggests that the TRANSP model is accurately redistributing particles spatially, but it does not redistribute the correct number of particles. Therefore, Kadomtsev reconnection appears to be an accurate representation of the observed redistribution. Instead, the discrepancy in the absolute magnitude of changes in the density arises due to kinetic effects of the energetic particles. In the TRANSP simulation, all beam ions inside the mixing radius participate in redistribution during the crash. However, from the experimental data and the OFSEF kinetic simulations, we see that this is not realistic; in general, redistribution of trapped particles is less severe than passing particles. Furthermore, fast-ion orbits are not distributed uniformly in space. Typically, the passing/trapped fraction is larger near the axis and decreases with larger major radius. The guiding-center orbit code mentioned earlier is used to map orbit boundaries for full-energy (75 keV) beam ions. Figure 14 shows orbit boundaries for full-energy beam ions just before a crash for shot 141182. Indeed, passing particles dominate in the core, and the passing/trapped fraction decreases quickly with increasing R. It becomes clear that a simulation that disregards kinetic effects and that mixes particles equally will underestimate the drop in fast-ion density in the core. In reality, the crash will interact mainly with the passing particles, kicking them from the core to larger R. In the meanwhile, according to the Kadomtsev model, particles near the $q = 1$ surface will be kicked inward toward the core. However, the majority of

particles near the $q = 1$ surface are those on trapped orbits and thus interact weakly with the instability. The net effect is a large drop in the core fast-ion density, as seen by FIDA. In the following, we discuss the particular aspects of fast-ion kinetic effects that differentiate the behavior of trapped and passing particles.

It is important to understand the dynamics which cause the difference in transport between ions of different orbit classifications during macroscopic MHD events. According to the theory in [23], the main drive for sawtooth-induced energetic-ion transport is the $\boldsymbol{E} \times \boldsymbol{B}$ drift associated with the induced electric field. In the ideal MHD framework (except for a thin layer about the reconnection surface), an electric field arises due to the bulk plasma motion during the crash event. Particles that remain attached to the perturbed flux surfaces $\boldsymbol{E} \times \boldsymbol{B}$ drift past the original (unperturbed) flux surfaces as the mode evolves. It is the finite $\boldsymbol{E} \times \boldsymbol{B}$ drift that tends to attach the particle to an evolving flux surface. However, three main mechanisms can be identified that compete with the $\boldsymbol{E} \times \boldsymbol{B}$ drift. Firstly, the relative size of a particle's orbit width Δr_{b} with respect to the sawtooth mixing radius r_{mix} affects the amount of time the particle spends in regions where the mode amplitude is strong; if Δr_{b} is comparable to or larger than r_{mix} the effect of the $\boldsymbol{E} \times \boldsymbol{B}$ drift on the particle orbit is weakened. Secondly, resonances between the characteristic frequency of the fundamental 1/1 mode (and higher harmonics) and characteristic ion orbit frequencies can cause enhanced transport. The mechanism for the enhanced transport in this case can also be identified as the $\boldsymbol{E} \times \boldsymbol{B}$ drift. However, the effect on a resonant particle manifests in less than one bounce period, leading instead to a larger orbit width. Thirdly, finite field curvature and field gradient drifts (collectively leading to toroidal drift) weaken particle attachment to evolving flux surfaces, lessening the effect of the $\boldsymbol{E} \times \boldsymbol{B}$ drift on the particle orbit. Although these three actions occur simultaneously, it is instructive to consider them independently. When $\Delta r_{\mathrm{b}} \approx r_{\mathrm{mix}}$, the particle spends a large fraction of its time in regions where the helical perturbation δB is weak. Thus the particle's poloidal-bounce/transit-averaged $\boldsymbol{E} \times \boldsymbol{B}$ drift associated with the induced electric field is reduced compared with spending all or most of its time inside the mixing radius ($\Delta r_{\mathrm{b}} < r_{\mathrm{mix}}$). On the other hand, a large orbit-width trapped ion may experience *enhanced* sawtooth-induced redistribution if its energy is sufficiently high to satisfy $s\omega_{\mathrm{b}} = n\omega_{\varphi}$ (where s is an integer, ω_{b} is the poloidal bounce/transit frequency, n is the toroidal mode number of the perturbation, and ω_{φ} is the toroidal precession frequency). In the case of sawteeth, a resonance can occur between the helical $n/m = 1/1$ mode (as well as higher n harmonics) and the particle orbit. If this occurs, the spatial excursions of the resonant trapped ion do not cancel on subsequent bounces resulting in a net displacement. However, during experiments on DIII-D in which neutral-beam injection is the only auxiliary heating method, the vast majority of fast ions have energies smaller than those required for resonances. An experimental demonstration of the resonant interaction between the sawtooth instability and RF-accelerated beam ions will be the subject of a future investigation. When the energy of energetic ions is less than the energy relevant for resonances,
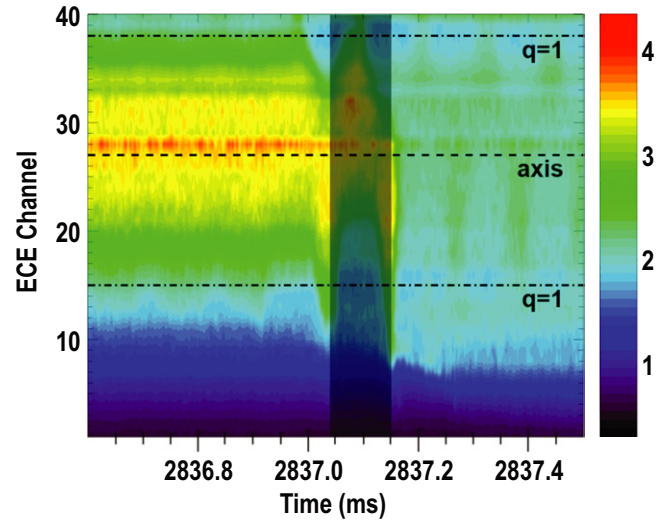
Figure 15. Contour plot of T_e as a function of ECE channel (where channel 1 is $(R, z) = (222, 0)$ cm and channel 40 is $(R, z) = (144, 0)$ cm) and time for a duration of 600 μs encompassing a typical sawtooth crash on shot 141182. The scale corresponds to T_e, and the core reaches a maximum value of 3.7 keV just before the crash. The shaded region ($\approx 100 \, \mu$s) corresponds to the crash phase when the core electron energy confinement deteriorates and presumably reconnection takes place.

the dominant mechanism differentiating passing and trapped particle transport is the toroidal drift due to field curvature and inhomogeneity. Next, we present a brief recapitulation of [23] showing the effect of toroidal drift on particle transport.

Toroidal drifts cause particles to deviate from the perturbed flux surfaces and to decouple from the evolving mode; a particle with sufficiently fast drift compared with the duration of the crash will trace out a toroidal drift surface and remain at a relatively constant minor radius. The influence of toroidal drifts can be interpreted analytically using a timescale approach. For the purposes here, the guiding-center velocity of a particle can be separated into four terms (see equation (5) in [23]): (1) particle velocity along the *unperturbed* flux surfaces, $v_{\parallel}^0$, (2) toroidal drift velocity, $v_{\mathrm{D}} \sim \rho v / 2R$ (where ρ is the Larmor radius, v is the particle velocity and R is the major radius of the particle location), (3) particle velocity along the helically *perturbed* flux surfaces, $v_{\parallel}^1$ and (4) mode-induced $\boldsymbol{E} \times \boldsymbol{B}$ drift velocity, v_E. To determine the influence of a crash on a particle's dynamics, three characteristic times should be considered: the crash duration τ_{cr}, the toroidal precession time (bounce-averaged toroidal period) τ_{pr} associated with v_{D}, and, for passing particles, the timescale of longitudinal motion (period around a *perturbed* flux surface) τ_{Ψ} associated with $v_{\parallel}^1$. Analytic formulae for τ_{pr} and τ_{Ψ} can be found in [23]. If the crash is sufficiently faster than a particle's toroidal drift period (i.e. $\tau_{\mathrm{cr}} \ll \tau_{\mathrm{pr}}$), the particle, well-coupled to a perturbed flux surface, moves with the evolving mode across the unperturbed flux surfaces due to the $\boldsymbol{E} \times \boldsymbol{B}$ drift. For a passing particle, however, even if its drift period is shorter than the crash duration, strong transport can occur provided its period about a perturbed flux surface is shorter than the drift period, i.e. $\tau_{\mathrm{pr}} \gg \tau_{\Psi}$. When this is the case, $v_{\parallel}^1$ dominates over v_{D} and the passing particle follows a perturbed flux surface.
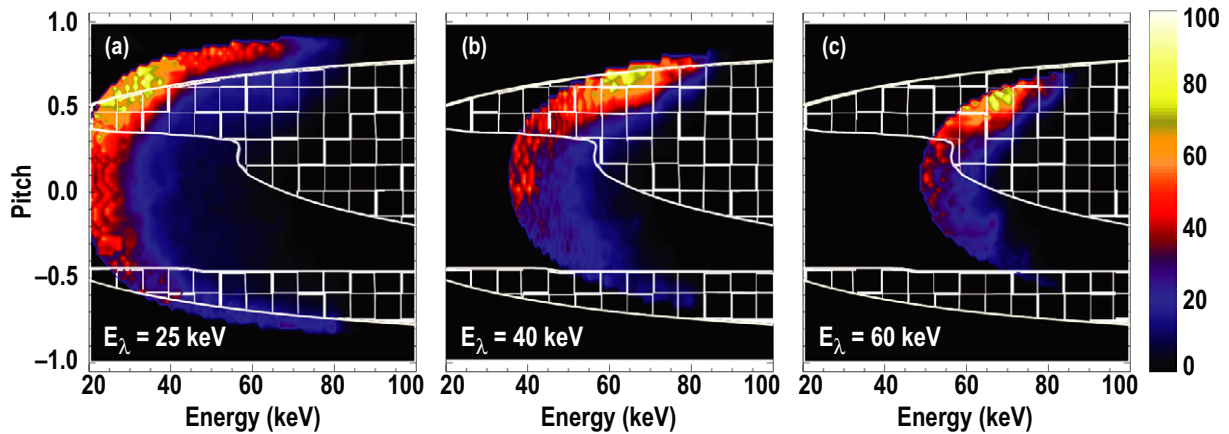
Figure 16. Velocity-space contribution to a vertical FIDA spectrum at $(R, z) = (183, 0)$ cm for measured energies E_λ of (*a*) 25 keV, (*b*) 40 keV and (*c*) 60 keV. The solid curve is E_{crit} and the hatched region is $E > E_{\text{crit}}$.

The previous timescale comparison can be reinterpreted in terms of more tractable experimental quantities: total particle energy E and particle pitch χ. A recasting of the passing and trapped redistribution criteria in terms of E and χ will allow us to display redistribution boundaries in our representation of velocity space. Along with the FIDA weight functions, the redistribution boundaries will give a sense as to how much of the FIDA signal is expected to be affected by a sawtooth crash. Since FIDA collects signal from volumes at the outboard midplane, the following analysis is restricted to poloidal angle $\theta = 0°$. We calculate the redistribution boundary in velocity-space starting with a precrash axisymmetric equilibrium. The conditions for strong redistribution, ($\tau_{\text{cr}} \ll \tau_{\text{pr}}$ and $\tau_\Psi \ll \tau_{\text{pr}}$) can be rewritten in terms of E and χ. In other words, there exists a pitch-dependent energy $E_{\text{crit}}(\chi)$ such that particles with total energy E *much less than* this critical value are strongly transported at the crash. The potential for transport depends on τ_{cr}, and the value is determined here by the time it takes the hot T_{e} core to be completely expelled to the periphery, as evidenced by ECE signals. Figure 15 is a contour plot of 40 midplane ECE channels during the last $600\,\mu$s of a typical sawtooth cycle for shot 141182. The mode becomes unstable around $t = 2837.00$ ms and the helical perturbation, evidenced by the precursor oscillation, grows until the hot core dissipates, and heat is ejected outside the $q = 1$ surface. The shaded region is presumably the crash phase initiating around 2837.05 ms where the helical displacement begins expelling heat outside $q = 1$. The core quickly cools, and after about $t = 2837.15$ ms, the crash has completed, flattening the T_{e} profile inside $q = 1$. Using this definition for the crash phase of several sawtooth crashes, the average τ_{cr} for shot 141182 is about $100\,\mu$s.

In order to calculate E_{crit}, τ_{pr} for passing and trapped and τ_Ψ for passing must be determined. The toroidal precession time τ_{pr} is calculated in an axisymmetric equilibrium by a guiding-center code that utilizes the adiabatic invariants of energy, magnetic moment and canonical toroidal momentum to constrain the particle motion; see the appendix in [19]. For passing particles the analytic approximation for τ_Ψ is obtained from equation (10) in [23]. The expressions $\tau_{\text{pr}} = \tau_\Psi$
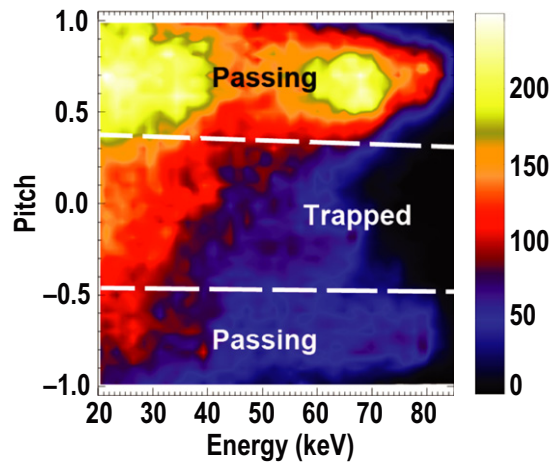
Figure 17. Slowing-down fast-ion distribution function at $(R, z) = (182, 0)$ cm computed by NUBEAM and TRANSP just before a typical sawtooth crash for shot 141182. Passing/trapped boundaries computed by a guiding-center code are overlaid dashed curves.

and $\tau_{\text{pr}} = \tau_{\text{cr}}$ (i.e. $E = E_{\text{crit}}$) are rewritten in terms of E and χ and plotted in figure 16 along with the weight functions of the vertical FIDA signal for spectral energies E_λ of 25, 40 and 60 keV. These velocity-space plots are generated by taking the convolution of the instrumental weight functions (recall figure 5) with a precrash fast-ion distribution function calculated by TRANSP. A contour plot of the precrash distribution function at the midplane and major radius $R = 182$ cm is shown in figure 17. The weight functions in figure 16 represent the contribution from velocity space to the measured spectrum at the particular spectral energy indicated. Recall the observation from figure 7 that the threshold in spectral energy for redistribution measured by the vertical system is $E_\lambda = 40$ keV. Therefore, it would be expected that the majority of the weight function corresponding to $E_\lambda = 40$ keV lies in the no-transport hatched region $E > E_{\text{crit}}$. Figure 16(*b*) suggests this is the case; only 40% of the signal at $E_\lambda = 40$ keV is in the transport $E < E_{\text{crit}}$ region. Another observation from figure 7 is that the spectrum is relatively unchanged by the sawtooth
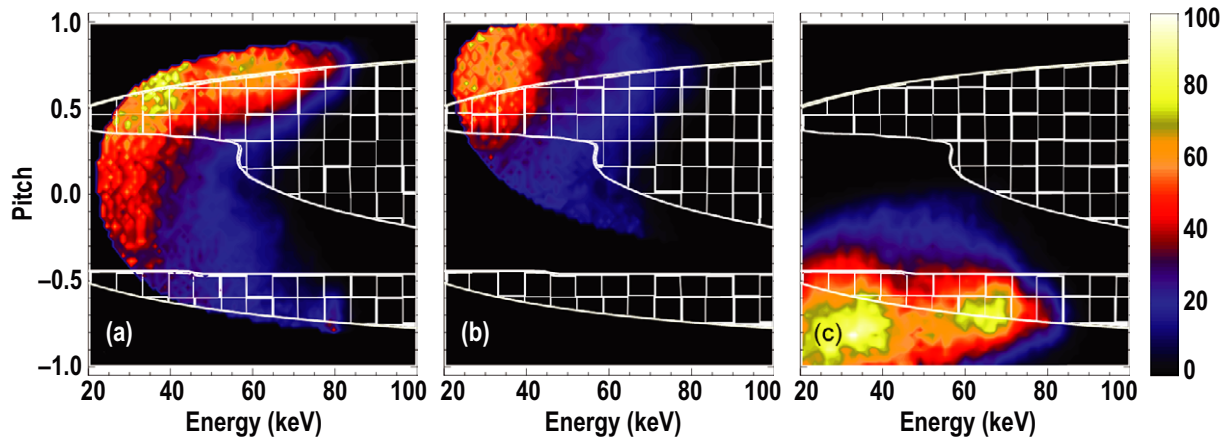
Figure 18. Velocity-space contribution to (*a*) the vertical signal for E_λ integrated 30–60 keV, (*b*) the near-tangential signal for E_λ integrated 30–60 keV, and (*c*) the 2D imaging signal for E_λ integrated 10–80 keV. The solid curve is E_{crit} and the hatched region is $E > E_{\text{crit}}$.

crash for Doppler shifts higher than $E_\lambda = 40$ keV. Figure 16(*c*) is the weight function for $E_\lambda = 60$ keV, and only 28% of the signal lies in the transport region $E < E_{\text{crit}}$. Conversely, portions of the spectrum with Doppler shifts smaller than $E_\lambda = 40$ keV are observed to be strongly affected. Figure 16(*a*) is the weight function for $E_\lambda = 25$ keV, and 65% of the signal is less than E_{crit}, consistent with the significant drop in the spectrum at that Doppler shift.

We apply this same interrogation to each of the three FIDA diagnostics to demonstrate the measured differences in transport reported earlier in figure 9. Figure 18 shows the velocity-space contribution to the FIDA signal for the three systems on shot 141182. The solid line denotes E_{crit}. Figure 18(*a*) is the phase-space contribution to an E_λ-integrated vertical signal ($E_\lambda = 30$–60 keV) for a core-localized viewing chord. Portions of the weight are lower than and greater than E_{crit}; about 52% of the velocity-space contribution lies below E_{crit}. Figure 18(*b*) is the phase-space contribution to an E_λ-integrated near-tangential signal ($E_\lambda = 30$–60 keV) for a viewing chord near the magnetic axis. About 77% of the weight lies below E_{crit} which is qualitatively consistent with the large core-density drop in the co-passing signal shown in figure 9. Similarly for the imaging system (figure 18(*c*)), about 73% of the velocity-space contribution lies below E_{crit}, also qualitatively consistent with the large drop observed in the counter-passing FIDA profile. Relatively speaking, the E_{crit} calculations qualitatively reproduce the observed result that the co- and counter-passing particles experience the strongest redistribution. In terms of absolute numbers, the changes to the signals predicted based on the analytic E_{crit} criterion are larger than those observed. Certainly a major contribution to this discrepancy is due to the physical process of the redistribution. The instability does not only cause a removal of some particles from a volume in phase space, but it leads to a mixing action; particles inside (outside) the $q = 1$ surface before the crash are transported outside (inside) $q = 1$ after the crash. The calculations above do not take the mixing into account; the percentages quoted are merely the fraction of the original population which satisfies the transport criteria. This analytic treatment of particle orbits reasonably predicts a critical energy at which toroidal drift

becomes crucial for determining the magnitude of particle redistribution.

4. Conclusions

The FIDA diagnostics at DIII-D have been utilized to study the phase-space dynamics of fast ions during a sawtooth crash. Spectral analysis indicates that trapped beam ions up to about 40 keV and all passing beam ions are redistributed during a sawtooth crash. The difference in transport is attributed to finite toroidal drift effects. While the $\boldsymbol{E} \times \boldsymbol{B}$ drift associated with the helical perturbation is responsible for driving transport (attaching particles to the evolving flux surfaces), an energetic ion decouples from the mode if its toroidal drift is strong enough. This naturally leads to the existence of a critical energy E_{crit} as a function of particle pitch angle. Particles with energy below E_{crit} are strongly redistributed by the sawtooth crash. Calculations of the critical energy are consistent with our observations of the 40 keV energy cutoff observed in the trapped particle spectrum.

Presumably, fast ions will behave differently in tokamaks with energetic-ion populations above typical NBI injection energies of about 100 keV. In ion-cyclotron-resonance-frequency heated discharges on JET, sawteeth are observed to have a strong effect on helium-3 minority ions with energies above the critical energy [25]. Although toroidal drift is strong for trapped and passing ions at very high temperatures ($\gg 100$ keV), effects due to resonances between trapped ions and the kink mode could become important [26]. Therefore, in tokamaks where the superthermal ion population is dominated by $\sim O(1\,\text{MeV})$ particles, the sawteeth may affect the trapped particles strongly. As the ions thermalize to $\sim O(100\,\text{keV})$, passing particles are dominantly transported; this is the regime studied in this paper. Further thermalization $\sim O(10\,\text{keV})$ leads to strong transport of both trapped and passing ions.

Acknowledgments

to extend our gratitude to R K Fisher, C T Holcomb, D C Pace, C C Petty, A D Turnbull and Y Zhu. Without their input and analysis efforts, this work would not have been possible. We also thank the entire DIII-D team for their tireless support and assistance.

References

[1] Marcus F B *et al* 1991 *Plasma Phys. Control. Fusion* **33** 277
[2] Zweben S J, Boivin R L, Duvall R E, Fredrickson E D, Goldston R J, Mynick H E, Strachan J D and White R B 1990 *Phys. Fluids* B **2** 1411
[3] Martin G, Jarvis O N, Kallne J, Merlo V, Sadler G and van Belle P 1987 *Phys. Scr.* **T16** 171
[4] Stratton B C, Fonck R J, McKee G R, Budny R V, Chang Z, Wising F and Odblom A 1996 *Nucl. Fusion* **36** 1586
[5] Petrov M P *et al* 1995 *Nucl. Fusion* **35** 1437
[6] Petrov M P *et al* 1996 *Proc. 16th IAEA Fusion Energy Conf. (Montreal, Canada)* (Vienna: IAEA)
[7] Nielsen S *et al* 2010 *Plasma Phys. Control. Fusion* **52** 092001
[8] Kolesnichenko Y I and Yakovenko Y V 1996 *Nucl. Fusion* **36** 159
[9] Luxon J L 2002 *Nucl. Fusion* **42** 614
[10] Lao L L, St John H, Stambaugh R D, Kellman A G and Pfeiffer W 1985 *Nucl. Fusion* **25** 1611.
[11] Rice B W, Burrell K H, Lao L L and Lin-Liu Y R 1997 *Phys. Rev. Lett.* **79** 2694

[12] Austin M E and Lohr J 2003 *Rev. Sci. Instrum.* **74** 1457
[13] Heidbrink W W, Taylor P L and Phillips J A 1997 *Rev. Sci. Instrum.* **68** 536–9
[14] Burrell K H, Kaplan D H, Gohil P, Nilson D G, Groebner R J and Thomas D M 2001 *Rev. Sci. Instrum.* **72** 1028
[15] Luo Y, Heidbrink W W, Burrell K H, Kaplan D H and Gohil P 2007 *Rev. Sci. Instrum.* **78** 033505
[16] Heidbrink W W, Luo Y, Burrell K H, Harvey R W, Pinsker R I and Ruskov E 2007 *Plasma Phys. Control. Fusion* **49** 1457
[17] Muscatello C M, Heidbrink W W, Taussig D and Burrell K H 2010 *Rev. Sci. Instrum.* **81** 10D316
[18] Van Zeeland M A, Heidbrink W W and Yu J H 2009 *Plasma Phys. Control. Fusion* **51** 055001
[19] Van Zeeland M A *et al* 2011 *Phys. Plasmas* **18** 056114
[20] Heidbrink W W, Liu D, Luo Y, Ruskov E and Geiger B 2011 *Commun. Comput. Phys.* **10** 716
[21] Pankin A, McCune D, Andre R, Bateman B and Kritz A 2004 *Comput. Phys. Commun.* **159** 157
[22] Ongena J, Evrard M, and McCune D 1998 *Trans. Fusion Technol.* **33** 181
[23] Kolesnichenko Y I, Lutsenko V V, Yakovenko Y V and Kamelander G 1997 *Phys. Plasmas* **4** 2544
[24] Kadomtsev B B 1975 *Sov. J. Plasma Phys.* **1** 710
[25] Jarvis O N, Adams J M, Howarth P, Marcus F B, Righi E, Sadler G J, Start D, Belle P V, Warrick C D and Watkins N 1996 *Nucl. Fusion* **36** 1513
[26] Kolesnichenko Y I, Lutsenko V V, White R B and Yakovenko Y V 2000 *Nucl. Fusion* **40** 1325